ELSEVIER

Contents lists available at ScienceDirect

Earth and Planetary Science Letters

www.elsevier.com/locate/epsl



Climate preconditions the Critical Zone: Elucidating the role of subsurface fractures in the evolution of asymmetric topography



Nicole West ^{a,*}, Eric Kirby ^b, Andrew A. Nyblade ^c, Susan L. Brantley ^{c,d}

- ^a Department of Earth and Atmospheric Sciences, Central Michigan University, United States
- ^b College of Earth Ocean and Atmospheric Sciences, Oregon State University, United States
- ^c Department of Geosciences, Pennsylvania State University, United States
- ^d Earth and Environmental Systems Institute, Pennsylvania State University, United States

ARTICLE INFO

Article history: Received 14 May 2018 Received in revised form 3 January 2019 Accepted 24 January 2019 Available online xxxx Editor: M. Bickle

Keywords: Critical Zone hillslope asymmetry shallow seismic frost-cracking

ABSTRACT

Although it has been long understood that rock properties strongly modulate the chemical and physical transformation of rock to regolith, recent studies highlight the central role of mechanical fracturing in the shallow subsurface. Competing hypotheses for how fractures co-evolve with surface processes suggest either that topographic stresses enhance or dampen the potential for fracture propagation, or alternatively suggest that fracture growth depends on the coupling between subsurface hydrology and weathering reactions. Both end-member models produce predictable and systematic spatial patterns of subsurface fracture distributions

To elucidate the processes responsible for the development of asymmetric hillslope topography and critical zone structure, we combine direct observations of subsurface fracture distributions in boreholes, indirect measures of subsurface rock properties inferred from seismic refraction surveys, and geochemical variations from subsurface samples at a small, shale-underlain catchment in central Pennsylvania. Our results reveal that seismic P-wave velocity profiles are consistent with subsurface fracture densities and zones of chemical depletion observed in boreholes, but that these distributions co-vary with hillslope aspect. Simple models of frost cracking show that, while modern climates are not conducive to subsurface segregation ice growth, asymmetric fracture distributions could have been achieved by subtle differences in aspect-related microclimates driving freeze-thaw during past periglacial climates. The spatial co-variance among fracture density, hillslope gradient, regolith depth, and regolith transport efficiency is consistent with chemo-mechanical damage arising from microclimatic conditions governing the long-term architecture of this watershed. Thus, damage driven by climate could explain the asymmetric topography observed today.

 $\ensuremath{\text{@}}$ 2019 Elsevier B.V. All rights reserved.

1. Introduction

Climate is well understood to be a primary factor governing landscape evolution (Gilbert, 1904; Rinaldo et al., 1995; Naylor and Gabet, 2007). For example, chemical weathering and dilational regolith transport both exhibit a dependence on temperature (Kirkby, 1967; White and Blum, 1995; West et al., 2005; Anderson et al., 2013). Likewise, first-order characteristics of the physical structure and evolution of landscapes manifest the interplay between diffusive and advective erosional regimes, which are strongly correlated to precipitation (e.g., Rinaldo et al., 1995; Perron et al., 2009). However, many of the details linking physical

* Corresponding author.

E-mail address: nicole.west@cmich.edu (N. West).

erosion and chemical weathering to climate remain unanswered (e.g., Raymo and Ruddiman, 1992; West et al., 2005).

Climate has long been invoked to explain observed differences in weathering and erosion on hillslopes of opposing aspect (e.g., Melton, 1960; Pierce and Colman, 1986; Naylor and Gabet, 2007). Here, differences in solar radiation received by hillslopes of opposing aspect drive sufficient differences in temperature and moisture availability to affect weathering and erosional processes (e.g., Pierce and Colman, 1986). Aspect-related differences in vegetation (e.g., Hack and Goodlett, 1960; Hinckley et al., 2014), soil moisture (Lin et al., 2006), weathering fluxes (Ma et al., 2013) and erosional efficiency (Anderson et al., 2013; West et al., 2013, 2014) have been reported across a variety of regional climatic regimes. Despite this attention, most studies of the critical zone subsurface stop at the soil-rock or soil-saprolite interface. Therefore, the control of

hillslope aspect on deep critical zone processes and the initiation of regolith production remains largely untested.

Recently, workers have begun to focus on the importance of rock fractures as pathways that guide meteoric water infiltration and facilitate chemical weathering in the subsurface (Riebe et al., 2017; Sullivan et al., 2016; Eppes and Keanini, 2017). Fractures also provide void space for biota to penetrate, accelerating weathering through chemical and physical processes (e.g., Hasenmueller et al., 2017). Microfractures can grow in massive bedrock via Fe-bearing mineral oxidation, as low-density HFO phases replace primary minerals in situ (Eggler et al., 1969; Fletcher et al., 2006). Additionally, frost-cracking is well-known to drive fracture propagation (Murton et al., 2006; Hales and Roering, 2007; Anderson et al., 2013), where water in the shallow subsurface breaks down bedrock by expansion during segregation ice growth. Finally, workers have begun to explore feedbacks between shallow stress perturbations set up by topography, tectonic stress and fracture growth (Miller and Dunne, 1996); recent studies argue that topographically induced stresses promote systematic variations in critical zone depth that co-varies with topography (e.g., St. Clair et al., 2015; Slim et al., 2015; Moon et al., 2017).

Geophysical techniques have long been exploited to visualize moisture patterns and fluid pathways in the shallow subsurface (Hubbard and Rubin, 2002), but recent years have seen a resurgence in the application of seismic wave propagation in the shallow subsurface to characterize the transitional boundaries between fresh and weathered bedrock (Holbrook et al., 2014). Because seismic velocities are dependent on the elastic properties (bulk and shear moduli) of Earth materials, in the shallowest parts of the crust, they provide constraints on in situ mineralogy, bulk density, and porosity. Variations in P-wave velocity have been shown to correspond with fracture density and distribution in the critical zone (e.g., Clarke and Burbank, 2011; Befus et al., 2011; Holbrook et al., 2014; Parsekian et al., 2015). Geophysical characterizations are further enhanced by comparisons with direct borehole observations, allowing for extrapolation of in situ point measurements of fracture and weathering depths to 2 and 3 dimensions (e.g., Orlando et al., 2015).

In this contribution, we combine subsurface observations from borehole and shallow seismic surveys to evaluate the hypothesis that microclimate variations govern deep critical zone structure and evolution in the Shale Hills Critical Zone Observatory (SSHO). Our previous research at the SSHO site demonstrated that systematic differences in the efficiency of dilational regolith creep on poleward- and equatorial-facing hillslopes can explain asymmetries in hillslope gradient, regolith thickness, and meteoric ¹⁰Be inventories (West et al., 2014). However, the question of whether such differences in efficiency could be sustained over geologic timescales remains unanswered. Here, we characterize the subsurface distribution of fracturing in the shale bedrock underlying the observatory and evaluate whether fracture distributions vary with hillslope aspect. We show how relatively subtle differences in thermal forcing driven by insolation on poleward- and equatorial-facing hillslopes could drive differences in the depth of frost cracking by segregation ice. Moreover, we show that these differences are not likely to be significant under present climates, and we infer that differences in fracture depth must be the legacy of periglacial conditions during previous glacial climates. Our results thus reveal a sensitive interplay between global climate, topography and microclimate that govern fracture propagation and facilitate the advance of weathering fronts. We suggest that preconditioning of the critical zone by ancient climate regimes may be a significant factor in mid-latitude and alpine regions globally.

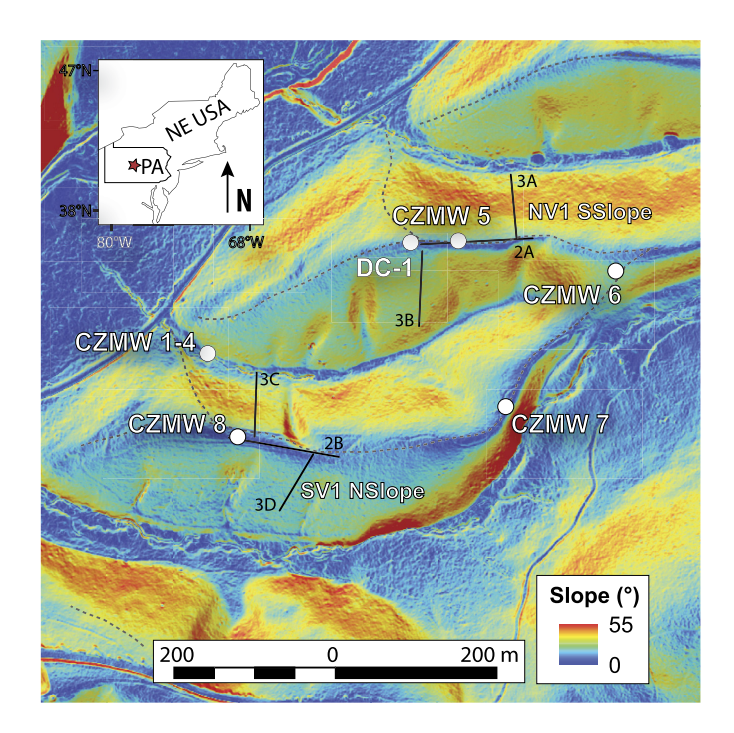


Fig. 1. Slope map overlain on a hillshade of the SSHO created from high resolution LiDAR topography (pasda.psu.edu), showing topographic asymmetry, with steeper north-facing slopes than south-facing slopes. Black lines correspond to seismic survey locations across the north and south ridges at SSHO. Black labels depict figure and panel numbers for corresponding seismic tomography. Borehole locations are indicated by white circles. White labels depict corresponding borehole numbers. CZMW 1-4 are plotted together due to their close proximity.

2. Critical Zone architecture at the Shale Hills CZO

The SSHO is located in the Valley and Ridge physiographic province of the Appalachian Mountains and currently experiences a temperate climate (MAP \sim 1 m/yr, MAT \sim 10 °C). SSHO contains three, small en echelon catchments (>0.1 km² each), developed entirely on the Rose Hill Shale, an Fe-rich, organic-poor shale deposited within the Appalachian Basin during the Silurian Period (Meyer et al., 1992). These SSHO watersheds are headwater catchments, bounded by ridges to the north and south, each containing westward-flowing ephemeral streams (Fig. 1). The watersheds formed into NE-SW striking strata (N54°E, Jin et al., 2010) that dip toward the NW (40°-88°, Sullivan et al., 2016). These hillslopes exhibit a pronounced topographic asymmetry, with north-facing slopes that are systematically 5-10° steeper than their southfacing counterparts (West et al., 2013, 2014); relief on these hillslopes is typically \sim 30 m. Field observations reveal that augerable regolith is thicker on north-facing hillslopes than south-facing hillslopes (Ma et al., 2013; West et al., 2013, 2014) and is underlain by a discontinuous layer of open-framework talus. Despite this asymmetry in hillslope gradient and regolith thickness, sediment fluxes determined from accumulation of meteoric ¹⁰Be within regolith (West et al., 2014) are similar on both north- and southfacing hillslopes (West et al., 2013); these relationships require that the efficiency of downslope transport is a factor of 2 greater along south-facing hillslopes. In modern climates, hillslopes in the SSHO experience more frequent freeze-thaw cycles on south-facing slopes, and these events appear to explain differences in transport efficiency (West et al., 2013).

Previous studies of the SSHO subsurface, using optical televiewer (OTV) logs from shallow and deep wells located along the ridges and valley floor (Fig. 1), indicate zones of bedrock fracture near the surface, decreasing with depth below land surface. Four wells located near the valley outlet reveal considerable fractur-

ing from the base of mobile soil (\sim 2.7 meters below land surface (mbls)) to 6 mbls, but below this depth, fracture density decreases toward the bottom of the boreholes at \sim 16 m (Kuntz et al., 2011; Slim et al., 2015; Sullivan et al., 2016). Fracture orientations reported by Sullivan et al. (2016) indicate that the majority of fractures orient subparallel to bedding, striking NE–SW, with the majority of fractures dipping WNW at 46 \pm 18°.

Previous geochemical studies at SSHO, presenting chemical and mineralogical observations taken from the deep borehole on the north ridge of the SSHO catchment (DC-1, Fig. 1), reveal a series of nested weathering fronts, i.e., depth intervals where minerals become depleted. Specifically, at roughly 6 mbls (meters below land surface), feldspar begins to dissolve and becomes depleted toward the surface, while at a depth of ~20 mbls, pyrite and carbonate minerals commence to dissolve (Jin et al., 2010; Brantley et al., 2013; Sullivan et al., 2016). Pyrite and carbonate minerals are almost 100% depleted above these depths under the northern ridge, and this pattern has also been observed in the borehole completed on the south ridge (\sim 16 mbls, Sullivan et al., 2016). Together, the observations of asymmetric topography and regolith transport efficiency, coupled with the apparent association between weathering fronts and fracture density, encourage the questions of what process drives fracture propagation beneath the SSHO watersheds, and how fracture distribution and regolith thickness vary with landscape position.

One potentially important consideration is that the central Appalachians have experienced a long history of freeze-thaw cycling, driven by periglacial climates associated with repeated glacial advances over the past \sim 2 Ma (Clark and Ciolkosz, 1988). During the Last Glacial Maximum (LGM, c. 21 kyr), for example, the Laurentide ice margin was located \sim 75 km north of SSHO. Hillslope soils developed during this time are inferred to record vigorous stirring and production of coarse detritus via frost shattering (Clark and Ciolkosz, 1988). Colluvial wedges of coarse, subangular debris are commonly found along toe slopes; some of these deposits are classified as greze litees - layered, unconsolidated deposits of oriented shale fragments inferred to have formed during solifluction (Clark and Ciolkosz, 1988). Although global scale models of Pleistocene climate suggest conditions conducive to intense frost cracking of bedrock in central Pennsylvania (Braconnot et al., 2012), the influence of these fluctuations in setting critical zone architecture has not been intensively investigated in this area, despite being invoked to explain subsurface flowpaths and deep weathering patterns at the SSHO (Sullivan et al., 2016).

3. Methods

To measure the depth and distribution of subsurface fractures at SSHO, we employed a combination of direct observations of fracture distributions in boreholes, following previous studies, with shallow seismic surveys along north- and south-facing hillslopes at SSHO. Shallow seismic refraction surveys were conducted on four hillslopes (2 north- and 2 south-facing) and along two ridgetops within and immediately adjacent to the Shale Hills CZO catchment during field campaigns completed in 2013 and 2015. Hillslope surveys were collected along linear transects, extending from the upper hillslope (near the ridgecrest) to the toe slope; transects are co-located along geochemical (Jin et al., 2010), U-series (Ma et al., 2013), and meteoric ¹⁰Be (West et al., 2013, 2014) sampling transects (Fig. 1). P-wave seismic data were collected using two Geometrics Geode data loggers/seismographs with a laptop controller (Seismodule Controller). In the 2013 campaign, 36 4.5 Hz sensors were used and 48 high-frequency sensors (40 Hz geophones) were used in 2015. We used a 10 lb sledgehammer and steel plate as the seismic source in both campaigns. On hillslopes within the SSHO (both north- and south-facing hillslopes), survey lengths were 96 m, running perpendicular to topographic contours, with 2 m geophone spacing. Ridgetop surveys followed the ridge axes, and extended to 115 m long, with a 5 m geophone spacing. Surveys were also collected just outside of the central SSHO watershed (over the ridge axes) to compare velocity structures among multiple hillslopes of north- and south-facing aspect. These surveys were 67 m long with 3 m geophone spacing. Each shot location comprised 5-stacked shots to minimize noise to signal ratio.

Seismic velocity inversions were conducted using the Geometrics SeisImager/2D software (Geometrics Inc., and OYO Inc.) and were calibrated against field observations and soil pit measurements. First arrival travel times for all seismic traces were manually picked (Fig. S1). From these first-arrivals, multi-layer initial models were constructed based on a simple time-term inversion of the time travel data, in which layer boundaries are visually identified based on pronounced changes in the travel-time slope, and layer velocities are based on least-square linear regressions to observed time travel data (Geometrics Inc.) (Fig. S2). Time term inversions for all seismic lines produced multi-layer models with upper layer velocities of <1 km/s and lower layer velocities of >2 km/s (Fig. S3). These initial models were then used for tomographic calculations. Models were verified against P-wave velocity profiles measured along exposed walls of soil pits completed near the toe slope of the south facing slope in the SSHO watershed, where layer thicknesses could be directly measured (Fig. S4).

For our direct calculations of subsurface fracture density, we used the subsurface fracture maps from 8 boreholes presented in Slim et al. (2015) and Sullivan et al. (2016), which used optical televiewer (OTV) imagery to characterize subsurface fractures at SSHO. In these studies, OTV logs were completed for four deep boreholes (~16 m) located in the SSHO valley floor (CZMW 1–4, previously described in Slim et al., 2015), three shallow boreholes located along the SSHO ridgelines (CZMW 5–7, ~6 m deep, Fig. S5), and one deep borehole located on the southern ridgeline of SSHO (CZMW8, ~24 m deep). Fractures were identified from OTV images in WellCad (Advanced Logic Technology), a software program that also measures fracture dip angle and azimuth. Additional details on OTV data collection at SSHO can be found in Slim et al. (2015) and Sullivan et al. (2016).

Because SSHO is comprised of soil-mantled hillslopes, with slopes and valleys overlain with alluvial and colluvial material (collectively referred to here as regolith), fracture depths observed in the boreholes needed to be corrected for overlying regolith thicknesses. Wells completed in the valley bottom were cased to just below the base of alluvium (\sim 3 mbls). Using augerable regolith depth measurements collected by West et al. (2013), we corrected the measured depth of subsurface fractures in all boreholes to represent the depth of fractures below the bedrock/soil interface.

When mapping fracture abundances, we also corrected for possible biased underestimation of steeply dipping fractures. The plane of steeply dipping fractures can be lost or cross-binned because of the shape and distance between the fracture segments, leading to underrepresentation in our fracture counts (e.g., Slim et al., 2015). Following Slim et al. (2015) we dip-weight the fractures counted in the ridgetop and valley wells by

$$W = \frac{1}{\cos \psi} \tag{1}$$

where W is the fracture count weight and ψ is the fracture dip angle in degrees.

Here, we complement previous borehole data collection by adding downhole geophysical analysis for the deep borehole completed on the southern ridge of the catchment (CZMW8, Fig. 1). Geophysical logs were collected using a MGX II and Matrix acquisi-

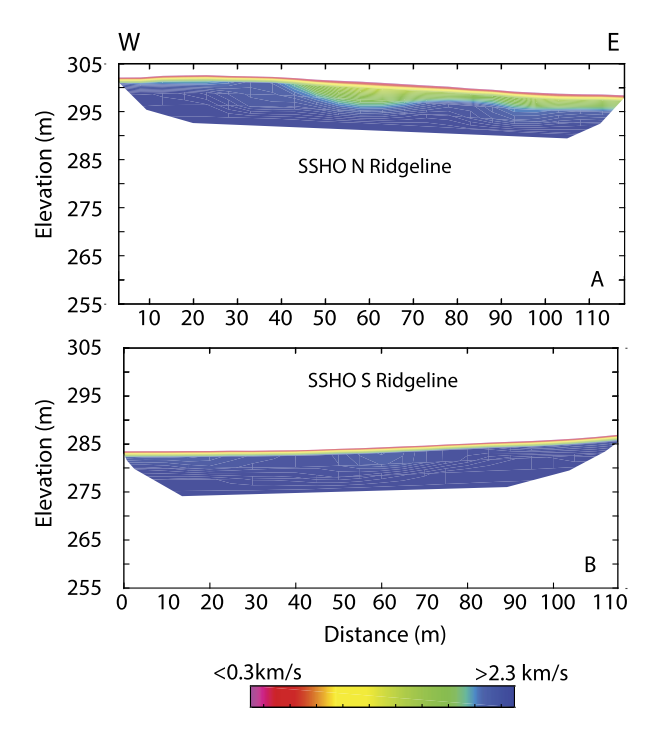


Fig. 2. Modeled P-wave tomography of the north and south ridgelines of the SSHO (A and B, respectively). Warmer colors correspond to low velocities and cooler colors correspond to fast velocities.

tion system (Mount Sopris Instrument Company) and include natural gamma, fluid temperature, specific conductance, 3-arm caliper, short and long resistivity, neutron, single point resistance, spontaneous potential, optical televiewer, acoustic televiewer, density and sonic data (Fig. S6).

4. Imaging Critical Zone architecture

4.1. Seismic surveys

Seismic refraction surveys were completed along north- and south-facing hillslopes at SSHO in order to elucidate the importance of aspect on the structure of the critical zone. All seismic tomographic inversions reveal three distinct layers with increasing depth in the subsurface (Figs. 2 and 3). The first is a thin layer of "slow" velocity material in upper decimeters of the subsurface, through which P-waves do not exceed velocities of \sim 0.6 km/s. The second layer is a "transition layer" in which material in the subsurface is characterized by a velocity gradient, where P-wave velocities increase from ~0.6 km/s to 2 km/s over relatively short depth intervals (\sim 2-4 m). The third layer is found at greatest depths (>8 mbls), and is comprised of uniformly "fast" velocity material, though which P-waves travel at velocities of 2-3 km/s. These patterns emerge regardless of the initial condition assumed for the tomographic inversion (Fig. S7), and thus they appear to represent robust characterizations of subsurface velocity structure.

Although the distributions of seismic velocity "layers" are observed along all sample transects, we find differences in the depth distributions of these layers on hillslopes with varying aspect. Refraction surveys consistently show that the "transition layer" along south-facing hillslopes is distributed over a relatively narrow depth range from $\sim\!0.5$ mbls–4 mbls, and the "slow" velocity layer is only observed in the uppermost 0.3–0.8 mbls (Fig. 3B and D). In contrast, along north-facing hillslopes, the "slow" velocity layer is considerably thicker, approaching $\sim\!2$ m, and the "transition layer" spans a greater depth range, from $\sim\!\!2$ to 10 mbls (Fig. 3A and C). This "transition layer" appears to thin toward the ridgecrest and valley floor within the Shale Hills Catchment.

Velocity measurements collected at hand-excavated soil pits within the SSHO reveal that P-wave velocities through soils range from 0.27–0.43 km/s and range from 2.12–3.57 km/s through in-

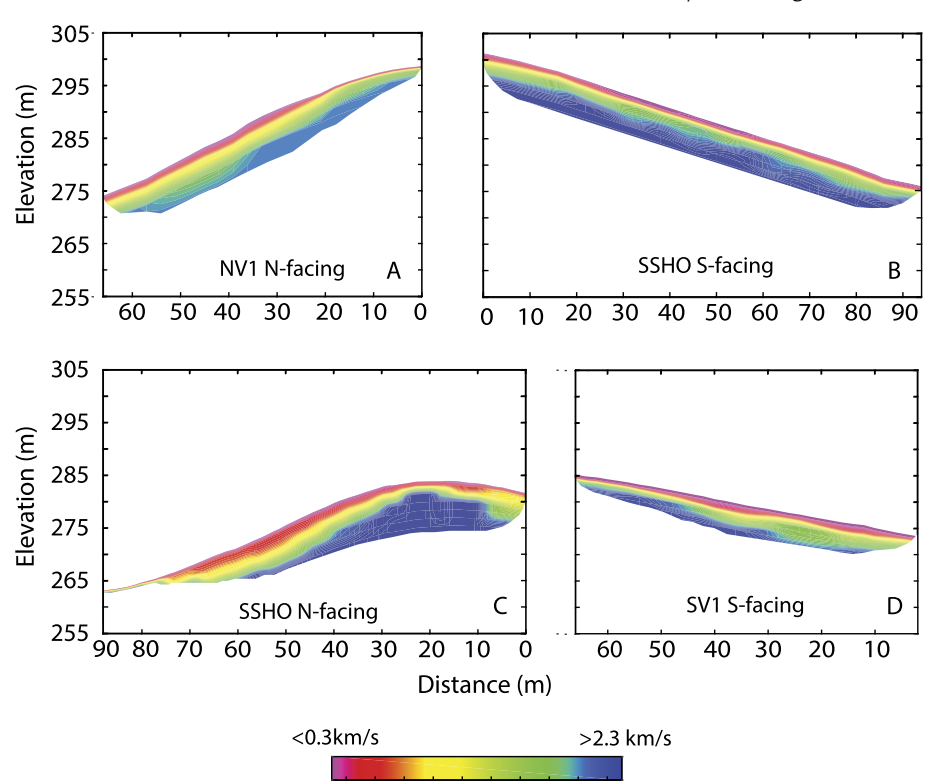


Fig. 3. Modeled P-wave tomography of the north- (A and C) and south-facing (B and D) hillslopes in and adjacent to the SSHO. Warmer colors correspond to low velocities and cooler colors correspond to fast velocities.

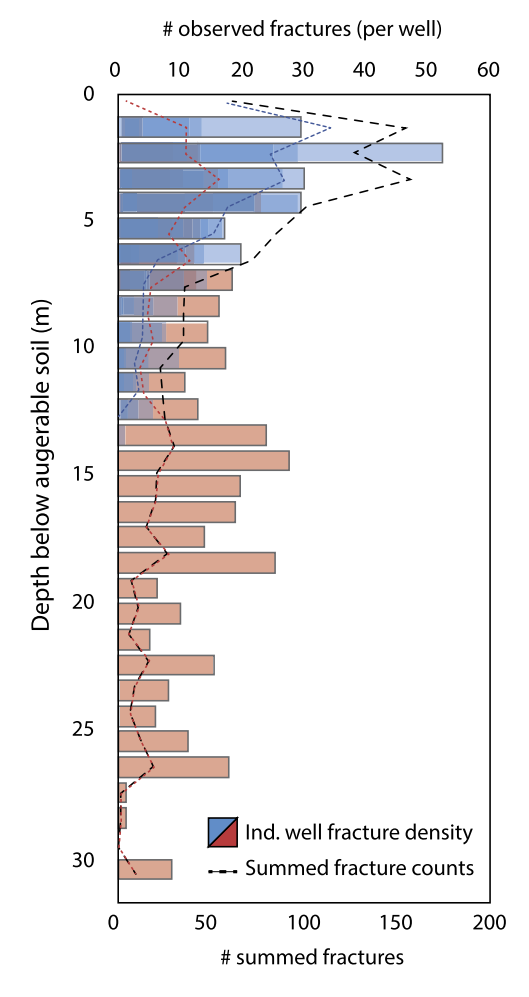


Fig. 4. Histogram of fracture occurrence by depth for all SSHO wells. Red bars show individual well fracture counts for ridgetop wells, blue bars represent valley floor wells. Histograms are overlain on one another to highlight zones of overlapping fracture density. Dashed lines show fracture counts by depth summed between wells, red for ridgetop wells, blue for valley wells, and black for all wells. All depths are corrected for overlying augerable regolith thicknesses reported in West et al. (2013). All wells show most fractures occur between 2 and 6 m below bedrock surface.

tact shale bedrock (Fig. S4). P-wave velocities measured through SSHO bedrock correspond well with reported P-wave velocities for intact shale from laboratory experiments (2.1 km/s-2.7 km/s, Press, 1966), suggesting that the observed regions with P-wave velocities >2 km/s at SSHO represent competent, intact bedrock. Similarly, P-wave velocities reported for soils and unconsolidated sediments range from 0.4-1.0 km/s (Befus et al., 2011), suggesting that zones of observed P-wave velocities <1 km/s at SSHO indeed represent regolith at or near the surface. Comparison of these velocity zones with auger thicknesses reported in West et al. (2013, 2014) and soil pit observations suggests that P-wave velocities less than 0.6 km/s correspond to the layer of regolith that is mobile under the current climate and vegetation regimes. Overall, P-wave velocity profiles at SSHO reveal uniformly thin regolith along south facing slopes, and thicker, more variable regolith depths along north-facing slopes, consistent with hand auger observations reported by West et al. (2013, 2014).

4.2. Direct observations in boreholes

Optical televiewer (OTV) logs of boreholes completed in the valley floor and along ridgetops at SSHO reveal that subsurface fractures are concentrated in the upper $\sim\!8$ m of bedrock (Fig. 4, Fig. S5). Peak fracture densities occur between 2 mbls and 5

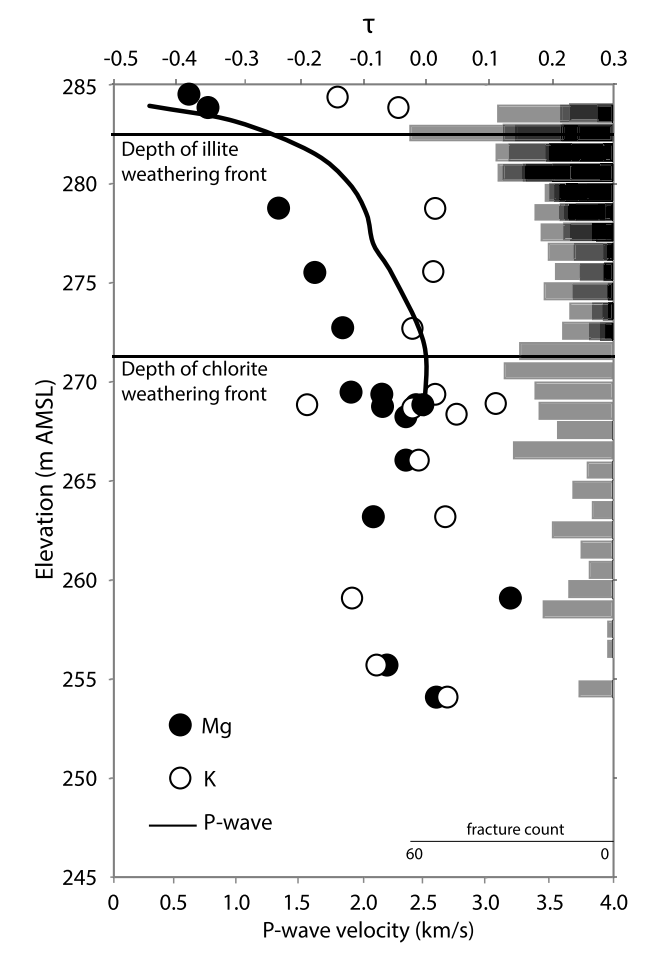


Fig. 5. Depth profile of average modeled 1D P-wave velocities proximal to the CZMW8 borehole on the south ridge of SSHO (black line) with values for the relative deficit in Mg (filled circles) and K (open circles) compared to protolith (τ) calculated for chips collected during drilling of CZMW8 (data from Sullivan et al., 2016). P-wave velocity line is truncated to the penetration depth of raypaths. Variation in τ around 0 indicates variability in parent composition. Stacked histograms of fracture counts from wells are shown as gray bars. τ is the mass transfer coefficient and is calculated based on well-established protocols described by Sullivan et al. (2016).

mbls for all wells located at both valley floor and ridgetop positions (Fig. 4). The main axis of the valley in the SSHO is overlain by 2–3 m of alluvial and colluvial material (West et al., 2013), whereas bedrock on ridgetops is covered by only several decimeters of regolith. Therefore, the depth of peak fracture density appears to be relatively uniform, despite regolith and/or alluvial cover. Absolute and peak fracture counts are, however, higher in the valley floor boreholes than in the ridgetop boreholes (Fig. 4).

Borehole geophysical logs of a deep well completed to 30 m in the south ridge of SSHO (CZMW8) reveal that in zones of high fracture density, P-wave velocities are reduced by up to 40% of those recorded through intact shale bedrock (Fig. S6). These results suggest that the observed P-wave transition zone in our refraction surveys may be representative of regions of high fracture density in the SSHO subsurface. The correlation between zones of high fracture density and zones of intermediate P-wave velocity provides compelling evidence that the P-wave transition zone represents a zone of fractured and possibly chemically altered bedrock.

These zones of dense fracturing are also zones where the bedrock has lost both magnesium and potassium (Mg and K, Fig. 5) compared to the underlying unweathered bedrock. These chemical losses are represented by the mass transfer coefficient tau,

$$\tau = \frac{C_{j,w}C_{i,p}}{C_{j,p}C_{i,w}} - 1$$

where $C_{j,w}$ and $C_{j,p}$ are the concentrations of the element of interest in weathered material and parent rock, respectively, and $C_{i,w}$ and $C_{i,p}$ are the concentrations of an immobile element in the weathered material and parent rock. Sampling and analysis details of τ data presented in Fig. 5 are discussed in Sullivan et al. (2016). Here, tau equals 0 when material has not weathered compared to parent and equals -1 when 100% of an element has been depleted compared to parent. Positive values of τ indicate addition of material compared to parent composition. To first order, depletion of these two elements are related to loss of chlorite (Mg) and illite (K), respectively, the two most common clay minerals in the Rose Hill shale (Jin et al., 2010). The correspondence of fracture density, P-wave velocity changes, and loss of illite and chlorite is striking. The co-occurrence of these observations is consistent with the interpretation that seismic measurements are mapping the depth of fracturing, and the depth of fracturing coincides with the depth of intense weathering of the clays. In addition, the base of the zone of peak fracture densities marks the initiation of dissolution of feldspar under the SSHO (Brantley et al., 2013).

5. Discussion

5.1. Fracture patterns at the SSHO

Our results reveal a striking correlation between the subsurface architecture of the SSHO and the topographic asymmetry in the watershed. As noted above, seismic surveys confirm that north-facing hillslopes are consistently mantled with thicker mobile regolith than south-facing ones across the SSHO (West et al., 2014). However, the data also reveal that the depth and thickness of the transitional boundary between rock and regolith covaries with hillslope aspect (Fig. 3). On north-facing slopes, the "transition layer" thickness varies from \sim 4 m to \sim 6 m (Fig. 3A and C), whereas it is uniformly <4 m thick along south-facing hillsides (Fig. 3B and D).

The correlation between P-wave velocities and fracture densities observed in boreholes completed along the ridgetops (Fig. 5) suggests that the P-wave transition zones along the hillslopes reflect zones of high fracture density. Efforts to understand the relationship between shallow rock fracture and topographic stresses (e.g., Miller and Dunne, 1996; Slim et al., 2015) suggest that focusing of stress along convex-upward valley bottoms should generate greater densities in bedrock shear fractures near valley bottoms relative to ridgetops. Although topographic stresses may explain the observation of higher fracture densities in valley bottom boreholes (e.g., Slim et al., 2015), they fail to predict the systematic differences in the depth of the velocity transition along north- and south-facing hillslopes. Similarly, more recent work incorporating regional tectonic stresses into models of stress accumulation in hilly topography suggests that in regions of compression similar to those occurring at SSHO, subsurface stress will mirror topography, resulting in failure potential highs that are deepest under ridges, and shallow under valleys, which should be observable as zones of low P-wave velocity (e.g., St. Clair et al., 2015; Moon et al., 2017). Our observations do not support this hypothesis, as transition layer depths are greatest under planar reaches of the north-facing hillslopes, and not under regions of high convexity or concavity as tectonic stress models predict (e.g., Slim et al., 2015; Moon et al., 2017).

These results and our previous inference of dilation-driven soil creep lead us to evaluate the role of aspect-related microclimate differences on fracture development. Specifically, we evaluate the potential for subsurface fracture initiation and growth via segregation ice. Ice lenses grow as liquid water held in surface tension (in

soil or porous rock) is drawn toward zones of freezing in the shallow subsurface by temperature induced capillary action (Hales and Roering, 2007; Murton et al., 2006; Marshall et al., 2015). Under permafrost conditions, segregation ice typically produces surface parallel fractures at the depth of the active layer (Murton et al., 2006). Although the depth for fracturing is strongly controlled by surface temperatures and the availability of water (Anderson et al., 2013; Hales and Roering, 2007; Rempel et al., 2016), most modeling efforts predict that frost cracking can be effective to depths greater than 10 mbls, peaking between 3 and 10 m in periglacial and permafrost conditions (Hales and Roering, 2007; Anderson et al., 2013; Rempel et al., 2016).

5.2. Evaluation of frost-cracking potential at SSHO

We calculate 1-dimensional frost cracking potentials at SSHO for both modern and potential periglacial climate conditions, using both modern measured surface soil temperature data from SSHO (Lin, 2014) and modeled surface temperature data from the Paleoclimate Modeling Intercomparison Project (phase 3, https://pmip3.lsce.ipsl.fr/; 50). Frost cracking potential (°C/cm-days) is the product of the subsurface temperature gradient and the time rock spends within the frost-cracking window, which is reported to exist between -8 and -3 °C (e.g., Hallet et al., 1991; Murton et al., 2006; Hales and Roering, 2007; Rempel et al., 2016). 1-dimensional annual thermal gradient models were constructed for SSHO using the equation:

$$T(z,t) = MAT + Tae^{-z\sqrt{\frac{\pi}{\alpha P_y}}} \sin\left(\frac{2\pi t}{P_y} - z\sqrt{\frac{\pi}{\alpha P_y}}\right)$$
 (2)

where T is temperature (°C), t is time, z is depth, MAT is mean annual temperature, Ta is the amplitude in annual temperature swings at the ground surface (°C), α is the thermal diffusivity of rock (900 °C cm⁻² d⁻¹ for shale, Clark, 1966), and P_y is period of the sinusoid (365 d). This model assumes exposed rock at the surface, and thus does not account for the insulating effects of soils or snowpack or water availability.

To model Pleistocene thermal gradients, we used modeled mean annual surface temperatures, which for central Pennsylvania are reported between 15 and $20\,^{\circ}\text{C}$ below modern MATs of $10\,^{\circ}\text{C}$ (Braconnot et al., 2012). Therefore, we present model results for MATs between 0 and $-10\,^{\circ}\text{C}$. We then apply a range of temperature swing amplitudes (Ta) from 5 to $20\,^{\circ}\text{C}$ and estimate the potential effects of aspect on frost-cracking potential, using observations reported from modern analogs.

Modern day climate conditions at SSHO are not cold enough to initiate frost cracking at any depth in the SSHO subsurface. However, when we consider temperatures that were likely characteristic of the periglacial conditions during the late Pleistocene, the depth of enhanced frost cracking potential extends to >10 m depth, with most model conditions generating peak frost cracking potentials deeper than 2 mbls (Fig. 6). Our model results suggest that annual temperature swings less than $10\,^{\circ}\text{C}$ do not generate frost cracking potential profiles that align with our observations. However, MATs from $-10-0\,^{\circ}\text{C}$, with swings of $10-20\,^{\circ}\text{C}$ can initiate frost-cracking via segregation ice growth in regions of the sub-surface that align with our peak fracture observations.

Comparing borehole observations and model predictions with geophysical surveys completed across the north and south ridgelines of SSHO shows that the base of the peak fracture zone corresponds to the initiation of decreasing P-wave velocity between 8 and 5 mbls (Fig. 5). These depths also correspond with our model predictions of peak frost cracking intensity. Thus, we infer that the depth of the "transition zone" in our seismic imagery of north- and south-facing hillslopes at SSHO may also correspond

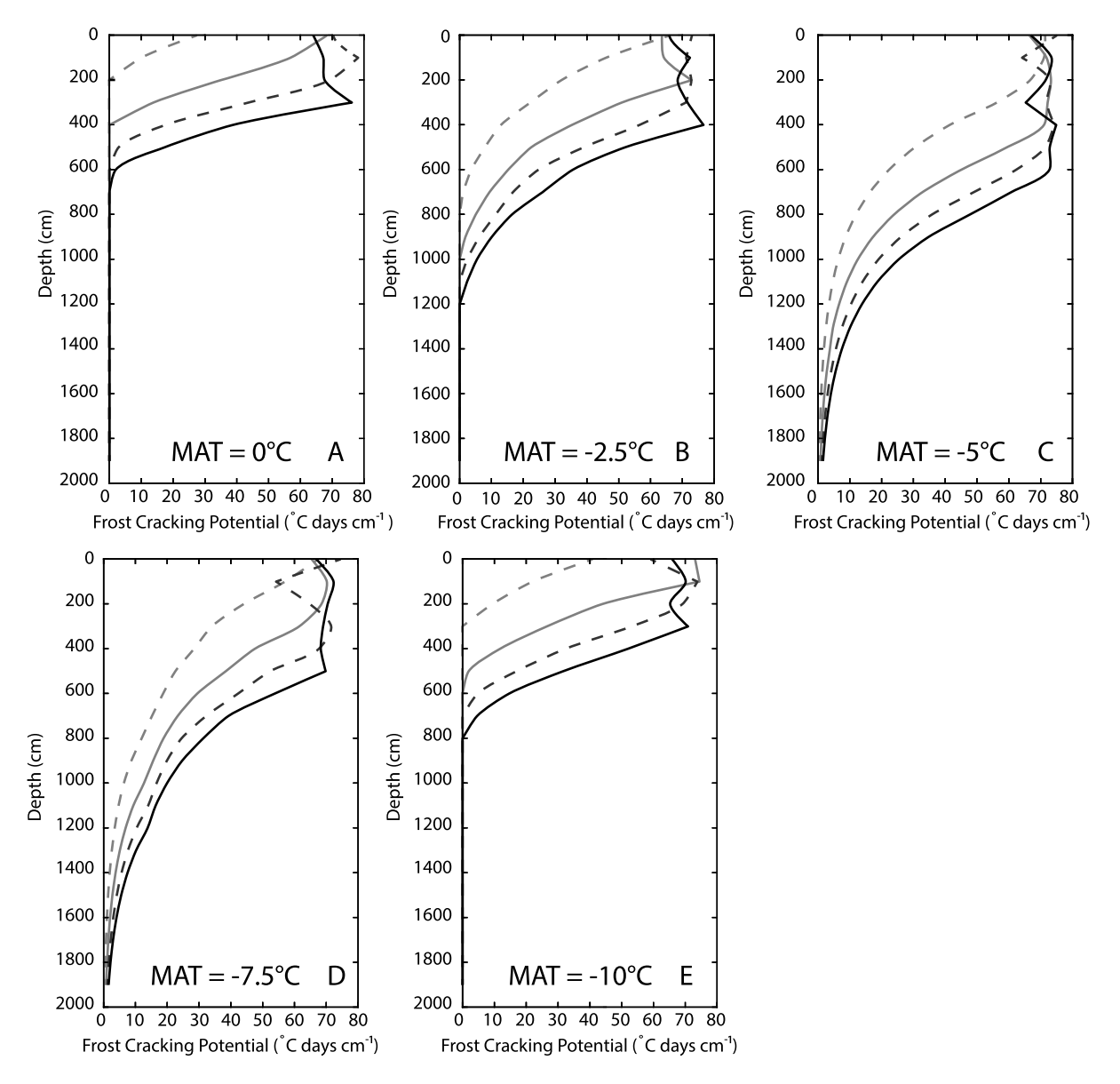


Fig. 6. Frost cracking model results for hypothetical periglacial conditions. For all panels, light gray dashed lines correspond to Ta = 5 °C, light gray solid lines correspond to Ta = 10 °C, dark gray dashed lines correspond to Ta = 20 °C, and black solid lines correspond to Ta = 20 °C, B) MAT = -2.5 °C, C) MAT = -5 °C, D) MAT = -7.5 °C, E) MAT = -10 °C. MATs derived from PMIP model outputs for 20 ka, and temperature amplitudes are estimated from modern periglacial soil data (Liu and Luo, 2011; Braconnot et al., 2012).

with depths of frost cracking, suggesting that aspect-related insolation differences may drive deeper fractures on slopes shielded from the sun.

In order to estimate differences in frost cracking potential with respect to aspect, we compare our model results to hillslope Pwave tomography as well as to conditions recorded in modern environments proximal to permafrost zones. The depths of P-wave transition on south-facing slopes at SSHO correlate most closely to modeled frost cracking potentials at -2.5 °C MAT. Alternatively, for north-facing slopes, MAT conditions that most closely correspond to P-wave transition zone depths are -5 and -7.5 °C. Intriguingly, these temperature values align with observations of surface temperatures in modern periglacial environments. On bare bedrock exposures near Fairbanks, AK, mean annual surface temperatures have been reported vary by up to 4°C between north- and southfacing hillslopes (Collins et al., 1988). Similarly, annual swings in surface temperature have been shown to be affected by aspect. On the Tibetan Plateau, surface soils have been reported to span temperature amplitudes of up to 15 °C for north-facing slopes and 17°C for south-facing slopes (Liu and Luo, 2011). These observations, combined with our model results and seismic tomography, lead us to conclude that frost-cracking via segregation ice growth may be the process driving the aspect-related asymmetries we observe in our seismic imagery.

$5.3.\ Frost\ shattering\ and\ the\ preconditioning\ of\ the\ SSHO\ Critical\ Zone$

Our combination of modeled MAT values for the SSHO region during the late Pleistocene with observed differences in surface temperatures associated with hillslope aspect predicts slight differences in the depth of fracture penetration between north-and south-facing slopes. Specifically, our models suggest that reduced insolation on north-facing slopes leads to lower average temperatures throughout the temperature profile that maintain temperatures well within the frost cracking window to somewhat greater depth than on south-facing slopes. We suggest that open-framework layers of shattered rock observed at the regolith/bedrock boundary on north-facing slopes in and around the

SSHO (West et al., 2013, 2014) are a manifestation of deeper penetration of frost shattering on these slopes during periglacial conditions associated with the Pleistocene glacial maxima (Braconnot et al., 2012).

A reasonable explanation for all of these observations is that frost shattering during periglacial periods at the SSHO "preconditioned" rocks in the near subsurface by generating a network of fractures. These fractures were subsequently exploited by shallow subsurface flow during the transition to warmer conditions during the late Pleistocene and Holocene. Along south-facing slopes, more frequent thawing events provided an efficient mechanism to transport coarse debris produced by frost shattering down hillslopes to the channel, where they could be conveyed out of the watershed (i.e., higher erosional efficiency). Conversely, on north-facing slopes, frost-shattered debris remained frozen, relatively immobile, and available for continued damage by frost action.

On both north- and south-facing hillslopes, fractures generated by ice provided pathways for penetration of meteoric fluids to depth, and may have dictated the initial depth of chemical reaction fronts. Given sufficient time, and subject to similar asymmetries in regolith transport efficiency during interglacial periods (West et al., 2014), these processes appear to have conspired to drive hillslopes toward their current topographic asymmetry. Our results thus reinforce the notion that asymmetry in Critical Zone architecture co-evolves with landscape topography as a consequence of microclimatic conditions (Anderson et al., 2013).

Our results also provide a plausible explanation for global observations of topographic asymmetry in mid-latitudes. Intravalley asymmetry is ubiquitous along the Western Cordillera between $\sim\!15$ and 50° latitude (e.g., Poulos et al., 2012), characterized by polar-facing hillslopes that stand steeper than their equatorial-facing counterparts. We attribute these first-order features of global topography to the interplay among microclimate, rock shattering, and erosional efficiency sustained throughout the glacial/interglacial cycles of the Pleistocene.

6. Conclusions

Geophysical surveys provide key insights into how processes occurring in Earth's shallow subsurface are fundamental to the structural evolution of the critical zone. Our results suggest that P-wave tomography provides information regarding the depth of fracturing that in the SSHO subsurface played an integral part in the physical and chemical evolution of the watershed. P-wave velocities reveal systematic differences in patterns of regolith and fracture thickness with respect to aspect at SSHO. The depth and spatial distributions of inferred fracture densities suggest that shattering of rock during periglacial conditions of the Pleistocene likely primed the hillslopes at SSHO for physical and chemical soil development during Holocene time. Fracturing during frost cracking events perhaps was a necessary driver for the observed aspectrelated topographic asymmetry and differences in chemical weathering on the north- and south-facing hillslopes at SSHO. The consistency between predicted frost-cracking during periglacial temperature conditions and observed fracture density patterns in both ridgetop and valley floor boreholes suggest the present-day architecture of the SSHO critical zone reflects the imposition of a prior climate history. Thus, it seems clear that the legacy of climate change and its impact on the landscape exerts a first-order control on the modern architecture and functioning of the Critical Zone.

Acknowledgements

This research was funded by National Science Foundation Grant EAR 13-31726 to S.L. Brantley. This research was conducted in Penn State's Stone Valley Forest, which is funded by the Penn

State College of Agriculture Sciences, Department of Ecosystem Science and Management and managed by the staff of the Forestlands Management Office. The authors thank N. Accardo for assistance in seismic modeling and J. Marshall, C. Regalla, and R. Lauer for discussions on frost cracking models. The authors also thank S. Mudd and one anonymous reviewer whose comments served to strengthen the presentation of our work.

Appendix A. Supplementary material

Supplementary material related to this article can be found online at https://doi.org/10.1016/j.epsl.2019.01.039.

References

- Anderson, R.S., Anderson, S.P., Tucker, G.E., 2013. Rock damage and regolith transport by frost: an example of climate modulation of the geomorphology of the critical zone. Earth Surf. Process. Landf. 38, 299–316. https://doi.org/10.1002/esp.3330.
- Befus, K.M., Sheehan, A.F., Leopold, M., Anderson, S.P., Anderson, R.S., 2011. Seismic constraints on critical zone architecture, Boulder Creek watershed, Front Range, Colorado, Vadose Zone J. 10, 915–927. https://doi.org/10.2136/vzj2010.0108.
- Braconnot, P., Harrison, S.P., Kageyama, M., Bartlein, P.J., Masson-Delmotte, V., Abe-Ouchi, A., Otto-Bliesner, B., Zhao, Y., 2012. Evaluation of climate models using palaeoclimatic data. Nat. Clim. Change 2 (6), 417–424. https://doi.org/10.1038/Nclimate1456.
- Brantley, S.L., Holleran, M.E., Jin, L., Bazilevskaya, E., 2013. Probing deep weathering in the Shale Hills Critical Zone Observatory, Pennsylvania (USA): the hypothesis of nested chemical reaction fronts in the subsurface. Earth Surf. Process. Landf. 38, 1280–1298. https://doi.org/10.1002/esp.3415.
- Clark Jr., S.P., 1966. Handbook of Physical Constants. GSA Mem., vol. 97.
- Clark, G.M., Ciolkosz, E.J., 1988. Periglacial geomorphology of the Appalachian highlands and interior highlands south of the glacial border – a review. Geomorphology 1, 191–220.
- Clarke, B.A., Burbank, D.W., 2011. Quantifying bedrock-fracture patterns within the shallow subsurface: implications for rock mass strength, bedrock landslides, and erodibility. J. Geophys. Res. 116 (F4).
- Collins, C.M., Haugen, R.K., Kreig, R.A., 1988. Natural ground temperatures in upland bedrock terrain, interior Alaska. In: Proceedings of the 6th International Conference on Permafrost, vol. 1. Trondheim, Norway, pp. 56–60.
- Eggler, D.H., Larson, E.E., Bradley, W.C., 1969. Granites, grusses, and Sherman erosion surface, southern Laramie Range, Colorado-Wyoming. Am. J. Sci. 267, 510–522.
- Eppes, M.-C., Keanini, R., 2017. Mechanical weathering and rock erosion by climate-dependent subcritical cracking. Rev. Geophys. 55, 470–508. https://doi.org/10.1002/2017RG000557.
- Fletcher, R.C., Buss, H., Brantley, S.L., 2006. A spheroidal weathering model coupling porewater chemistry to soil thicknesses during steady-state denudation. Earth Planet. Sci. Lett. 244 (1–2), 444–457. https://doi.org/10.1016/j.epsl.2006.01.055.
- Gilbert, G.K., 1904. Systematic asymmetry of crest lines in the High Sierra of California. J. Geol. 12, 579–588. https://doi.org/10.1086/621182.
- Hack, J.T., Goodlett, J.C., 1960. Geomorphology and forest ecology of a mountain region in the Central Appalachians. U. S. Geol. Surv. Prof. Pap. 347. 66 p.
- Hales, T.C., Roering, J.J., 2007. Climatic controls on frost cracking and implications for the evolution of bedrock landscapes. J. Geophys. Res. 112, F02033. https:// doi.org/10.1029/2006/F000616.
- Hallet, B., Walder, J., Stubbs, C.W., 1991. Weathering by segregation ice growth in microcracks at sustained sub-zero temperatures: verification from an experimental study using acoustic emissions. Permafr. Periglac. Process. 2, 283–300.
- Hasenmueller, E., Gu, X., Weitzman, J., Adams, T., Stinchcomb, G., Eissenstat, D., Drohan, P., Brantley, S., Kaye, J., 2017. Weathering of rock to regolith: the activity of deep roots in bedrock. Geoderma 300, 11–31.
- Hinckley, E.S., Ebel, B.A., Barnes, R.T., Anderson, R.S., Williams, M.W., Anderson, S.P., 2014. Aspect control of water movement on hillslopes near the rain-snow transition of the Colorado Front Range. Hydrol. Process. 28 (1), 74–85. https://doi.org/10.1002/hyp.9549.
- Holbrook, W.S., Riebe, C.S., Elwaseif, M., Hayes, J.L., Basler-Reeder, K., Harry, D.L., Malazian, A., Dosetto, A., Hartsough, P.C., Hopmans, J.W., 2014. Geophysical constraints on deep weathering and water storage potential in the Southern Sierra Critical Zone Observatory. Earth Surf. Process. Landf. 39, 366–380. https:// doi.org/10.1002/esp.3502.
- Hubbard, S.S., Rubin, Y., 2002. Hydrogeophysics: state of the discipline. Eos 83 (51), 602-606
- Jin, L., Ravella, R., Ketchum, B., Bierman, P.R., Heaney, P., White, T., Brantley, S.L., 2010. Mineral weathering and elemental transport during hillslope evolution at the Susquehanna/Shale Hills Critical Zone Observatory. Geochim. Cosmochim. Acta 74, 3669–3691.
- Kirkby, M.J., 1967. Measurement and theory of soil creep. J. Geol. 75 (4), 359–378. Kuntz, B., Rubin, S., Berkowitz, B., Singha, K., 2011. Quantifying solute transport at the Shale Hills Critical Zone Observatory. Vadose Zone J. 10, 843–857.

- Lin, H., 2014. CZO dataset: Shale Hills hydropedologic properties, soil temperature (2007–2014). http://criticalzone.org/shale-hills/data/dataset/2587/.
- Lin, H., Kogelmann, W., Walker, C., Bruns, M.A., 2006. Soil moisture patterns in a forested catchment: a hydropedological perspective. Geoderma 131, 345–368.
- Liu, Xinsheng, Luo, T., 2011. Spatiotemporal variability of soil temperature and moisture across two contrasting timberline ecotones in the Sergyemla Mountains, Southeast Tibet. Arct. Antarct. Alp. Res. 43 (2), 229–238.
- Ma, L., Chabaux, F., Jin, L., West, N., Kirby, E., Brantley, S., 2013. Regolith production and transport at the Susquehanna Shale Hills Critical Zone Observatory – Part 1: insights from U-series isotopes. J. Geophys. Res., Earth Surf. 118. https://doi. org/10.1002/jgrf.20037.
- Marshall, J.A., Roering, J.J., Bartlein, P.J., Gavin, D.G., Granger, D.E., Rempel, A.W., Praskievicz, S.J., Hales, T.C., 2015. Frost for the trees: did climate increase erosion in unglaciated landscapes during the late Pleistocene? Sci. Adv. 1 (10), e1500715. https://doi.org/10.1126/sciadv.1500715.
- Melton, M.A., 1960. Intravalley variation in slope angles related to microclimate and erosional environment. Geol. Soc. Am. Bull. 71, 133–144. https://doi.org/10.1130/ 0016-7606(1960)71[133:IVISAR]2.0.CO;2.
- Meyer, S.C., Textoris, D.A., Dennison, J.M., 1992. Lithofacies of the Silurian Keefer Sandstone, east-central Appalachian basin, USA. Sediment. Geol. 76, 187–206.
- Miller, D.J., Dunne, T., 1996. Topographic perturbations of regional stresses and consequent bedrock fracturing. J. Geophys. Res., Solid Earth 101 (B11), 25523–25536.
- Moon, S., Perron, J.T., Martel, S.J., Holbrook, W.S., St. Clair, J., 2017. A model of three-dimensional topographic stresses with implications for bedrock fractures, surface processes, and landscape evolution. J. Geophys. Res., Earth Surf. 122 (4), 823–846. https://doi.org/10.1002/2016JF004155.
- Murton, J.B., Peterson, R., Ozouf, J.C., 2006. Bedrock fracture by segregation ice growth in cold regions. Science 314 (5802), 1127–1129.
- Naylor, S., Gabet, E.J., 2007. Valley asymmetry and glacial versus nonglacial erosion in the Bitterroot Range, Montana, USA. Geology 35, 375–378. https://doi.org/10. 1130/G23283A.1.
- Orlando, J., Comas, X., Hynek, S.A., Buss, H.L., Brantley, S.L., 2015. Architecture of the deep critical zone in the Río Icacos watershed (Luquillo Critical Zone Observatory, Puerto Rico) inferred from drilling and ground penetrating radar (GPR). Earth Surf. Process. Landf. 41 (13), 1826–1840. https://doi.org/10.1002/esp.3948.
- Parsekian, A.D., Singha, K., Minsley, B.J., Holbrook, W.S., Slater, L., 2015. Multiscale geophysical imaging of the critical zone. Rev. Geophys. 53. https://doi.org/10. 1002/2014RG000465.
- Perron, J.T., Kirchner, J.W., Dietrich, W.E., 2009. Formation of evenly spaced ridges and valleys. Nature 460, 502–505.

- Pierce, K.L., Colman, S.M., 1986. Effect of height and orientation (microclimate) on geomorphic degradation rates and processes, late glacial terrace scarps in central Idaho. Geol. Soc. Am. Bull. 97, 869–885. https://doi.org/10.1130/0016-7606(1986)97<869:EOHAOM>2.0.CO;2.
- Poulos, M.J., Pierce, J.L., Flores, A.N., Benner, S.G., 2012. Hillslope asymmetry maps reveal widespread, multi-scale organization. Geophys. Res. Lett. 39, L06406. https://doi.org/10.1029/2012GL051283.
- Press, F., 1966. Seismic velocities. In: Clark Jr., S.P. (Ed.), Handbook of Physical Constants. In: GSA Mem., vol. 97, pp. 195–218.
- Raymo, M.E., Ruddiman, W.F., 1992. Tectonic forcing of late Cenozoic climate. Nature 359 (6391), 117–122. https://doi.org/10.1038/359117a0.
- Rempel, A.W., Marshall, J.A., Roering, J.J., 2016. Modeling relative frost weathering rates at geomorphic scales. Earth Planet. Sci. Lett. 453, 87–95.
- Riebe, C.S., Hahm, W.J., Brantley, S.L., 2017. Controls on deep critical zone architecture: a historical view and four testable hypotheses. Earth Surf. Process. Landf. 42 (1), 128–156. https://doi.org/10.1002/esp.4052.
- Rinaldo, A., Dietrich, W.E., Rigon, R., Vogel, G.K., Rodriguez-Iturbe, I., 1995. Geomorphological signatures of climate. Nature 374, 632–635.
- Slim, M., Perron, J.T., Martel, S.J., Singha, K., 2015. Topographic stress and rock fracture: a two dimensional numerical model for arbitrary topography and preliminary comparison with borehole observations. Earth Surf. Process. Landf. 40 (4), 512–529.
- St. Clair, J., Moon, S., Holbrook, W.S., Perron, J.T., Riebe, C.S., Martel, S.J., Carr, B., Harman, C., Singha, K., de Richter, D.B., 2015. Geophysical imaging reveals topographic stress control of bedrock weathering. Science 350 (6260), 534–538.
- Sullivan, P.L., Hynek, S., Gu, X., Singha, K., White, T., West, N., Kim, H., Clarke, B., Kirby, E., Duffy, C., Brantley, S.L., 2016. Oxidative dissolution under channel leads geomorphological evolution at the Shale Hills Catchment. Am. J. Sci. 316, 981–1026. https://doi.org/10.2475/10.2016.02.
- West, A.J., Galy, A., Bickle, M., 2005. Tectonic and climatic controls on silicate weathering. Earth Planet. Sci. Lett. 235 (1–2), 211–228.
- West, N., Kirby, E., Bierman, P., Slingerland, R., Ma, L., Rood, D., Brantley, S., 2013. Regolith production and transport at the Susquehanna Shale Hills Critical Zone Observatory, Part 2: insights from meteoric ¹⁰Be. J. Geophys. Res. 118 (3), 1877–1896. https://doi.org/10.1002/jgrf.20121.
- West, N., Kirby, E., Bierman, P., Clarke, B.A., 2014. Aspect-dependent variations in regolith creep revealed by meteoric ¹⁰Be. Geology 42 (6), 507–510. https://doi.org/10.1130/G35357.1.
- White, A.F., Blum, A.E., 1995. Effects of climate on chemical weathering in watersheds. Geochim. Cosmochim. Acta 59 (9), 1729–1747.